Hindawi
Advances in Civil Engineering
Volume 2024, Article ID 6632239, 18 pages
https://doi.org/10.1155/2024/6632239

Research Article

Study on Mechanical Model for Postpeak Shear Behavior of Rock Joints Based on Degradation Characteristics of the 3D Morphology

Juan Liu,[1] Feng Gao ,[1,2] Yan Xing,[2] and Xianghe Gao[1]

[1]*State Key Laboratory for Geomechanics and Deep Underground Engineering, China University of Mining and Technology, Xuzhou 221116, China*
[2]*Department of School of Mechanics and Civil Engineering, China University of Mining and Technology, Xuzhou 221116, China*

Correspondence should be addressed to Feng Gao; gfengcumt@126.com

Received 29 August 2023; Revised 3 January 2024; Accepted 9 January 2024; Published 12 March 2024

Academic Editor: Ma Jianjun

The 3D morphology of the joint surface significantly influences the shear behavior of the jointrock. Constant normal load (CNL) direct shear tests with different shear displacement were conducted to understand the shear stress changing with joint roughness and damage degree during shear. The rough joint specimens were prepared using 3D scanning and printing techniques, and shear tests with different normal stresses and shear displacements were performed. Four different parameters and the damaged area quantitatively described by the image binarization and box dimension were calculated and compared to study the roughness evolution of joint surfaces. The experimental results demonstrated that the roughness parameter and shear stress decrease and approach constant values with increasing shear displacement. A JRC degradation model was presented based on regression analyses to evaluate the JRC values of rock joints under various displacements to replace it in the JRC–JCS model. Additionally, a new postshear behavior modeling was proposed for rock joints based on surface degradation characteristics under various initial joint roughness coefficients (JRC_0) and normal stress. The stress–displacement curves resulting from the proposed modified model work well in predicting the postpeak stress–displacement curve, which can prove the effectiveness of the postpeak shear behavior modeling.

1. Introduction

The engineering rock mass is a multifracture body formed by the longitudinal and transverse geological structure planes [1], as shown in Figure 1. The characteristics of a jointed rock mass are determined rather by the joints of the rock system than on the property of the intact rock mass. The presence of multiple fracture directly impacts the macromechanical characteristics of the rock bodies, such as load resistance, deformation characteristics, shear strength, and damage mode [2–4]. Any morphological changes in the structural face may cause deformation and destabilization of the rock bodies [5, 6]. Therefore, it is essential to investigate the roughness parameters of rock joints in the failure process.

The morphology of the internal structures and joints is gradually worn out because of the loading action on the engineering rock mass [10, 11]. Meanwhile, the damage mechanism of engineering rock masses is almost related to the damage and wear of the joint surfaces under shear conditions [12, 13]. Li et al. [14] proposed a model focusing on asperity degradation and debris backfilling during a complete shear cycle. The roughness of the joint surfaces changes with the shear displacement (u) leading to changes in mechanical properties [15]. Hence, a clear understanding of the damaged extent and joint morphology during shearing is essential to study the engineering structural stability.

Joint surface is composed of many peaks and valleys with different shapes and sizes, and these asperities' deformations cause macroscopic failures during shearing. Therefore, describing the surface features is a critical factor in studying the shear mechanics of joints. Many quantitative approaches were proposed to quantify the roughness of rock joints [16, 17]. The

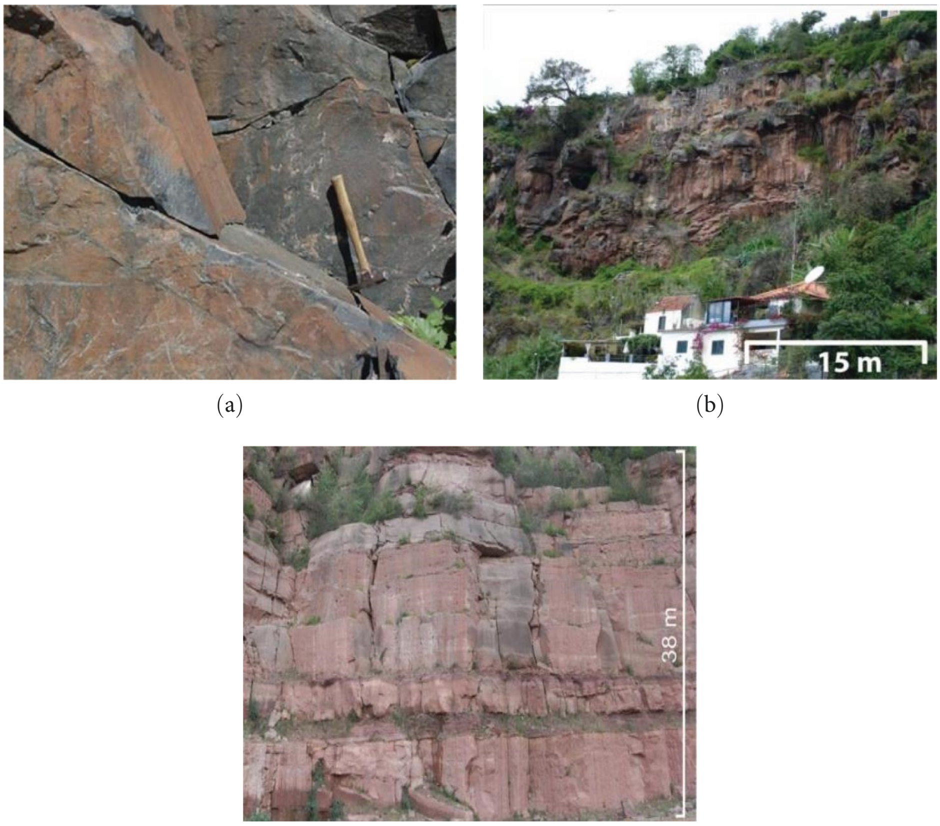

(a) (b) (c)

Figure 1: Rock mass with geological structure planes: (a) rock cut containing fracture traces facets [7]; (b) exposed slopes [8]; and (c) Quarry Rockenau [9].

parameters can be mainly divided into two directions. The first kind is the fractal dimension [18], such as D_c (fractal dimension determined by the compass-walking method) [19]. The other is the statistical parameter, such as σ_i (standard deviation of the angle) [20].

The morphological features of rock joints are anisotropic due to the size, angle, and undulation variations for asperities [21]. No two samples of natural rock joints, even from the same deposit, are identical [22, 23]. It is difficult to obtain joint samples with identical physical surface pattern to perform tests under same conditions [24–26]. Consequently, the jointed cast samples by similar materials were used to study the impact of morphological factors on shear behaviors. Recently developed three-dimensional (3D) scanning and 3D printing techniques offer a new approach for manufacturing laboratory samples with the same uneven joint surfaces [27, 28]. Jiang et al. [22] proposed a way to batch-produce rock joints with the same natural surfaces through 3D optical scanning of original rock joint specimens to gain their digitally natural geometry.

Considering these, experimental methods were developed to analyze the impact of the normal stress (σ_n) and u on the joints' damage extent. The surfaces with natural morphological joints were obtained by 3D scanning and printing technology, and the joint samples with similar materials were cast. Based on direct shear tests, the anisotropic damage of the joint surface was investigated by four kinds of parameters at different u. The damaged area was quantitatively described by the fractal dimension of joints' binary image. The experimental results demonstrated that the joint roughness and shear stress decrease after peak shear strength and approach a constant value with u increasing. The JRC degradation model was presented based on regression analyses to evaluate the JRC values of rock joints under various displacements to replace it in the JRC–JCS model. Based on surface degradation characteristics, we proposed postshear behavior modeling for rock joints, proving the effectiveness of postpeak shear behavior modeling according to the relations between the JRC and u.

2. Experimental Methodology

2.1. Mechanical Parameters of Red Sandstone Samples. The testing samples were red sandstone from Linyi, Shandong, China. The samples were processed with 100 mm × 100 mm × 100 mm and flattened by the grinder. The surface of each sample is flat without visible defects to ensure constant stress. According to the X-ray diffractogram shown in Figure 2, the red sandstone primarily comprises quartz, feldspar, mica, and pyrite.

The shear experiments were performed to study the effect of joint roughness and contact areas on shear behavior. A direct shear system (TAWD-2000) was used in this search,

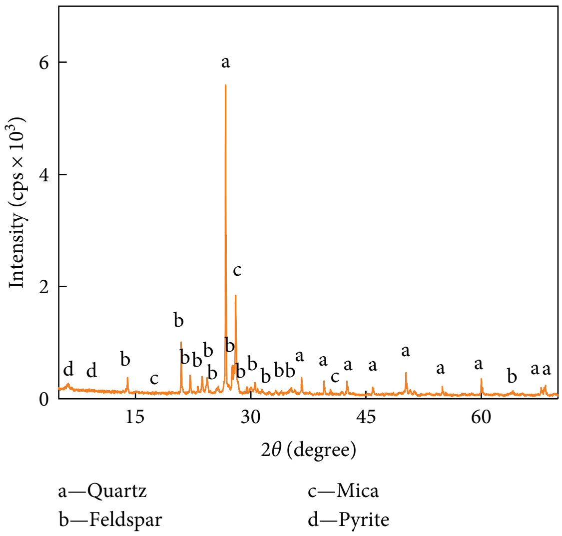

Figure 2: X-ray diffraction pattern of red sandstone [29].

as shown in Figure 3. The maximum axial load of the machine is 2,000 kN, and the measurement accuracy is $\pm 1\%$; the measurement range of the axial displacement is 0–100 mm, and the measurement accuracy is $\pm 0.5\%$; the measurement range of the axial deformation is 0–10 mm, and the measurement accuracy is $\pm 0.5\%$. The maximum tangential load is 1,000 kN, minimum tangential load is 10 kN, and the measurement accuracy is $\pm 1\%$; the measurement range of the shear displacement is 0–100 mm, and the measurement accuracy is $\pm 0.5\%$; the measurement range of the shear deformation is 0–25 mm, and the measurement accuracy is ± 0.001 mm.

Before the test, prestress (2 kN) was applied in normal and shear directions. Then, $\sigma_n = 5.0$ MPa was applied with a 0.2 min/mm loading rate. Subsequently, the shear stress was applied with the loading rate of 0.2 min/mm with constant normal load (CNL). And the experimental results are shown in Figure 4.

The 3D point cloud data of the joint surface were scanned by VR-5000 (Figure 5). It was produced by KEYENCE (CHINA), consisting of an X–Y–Z positioning table and a laser scan micrometer. The imaging principle of the VR-5000 is shown in Figure 6.

2.2. Determination of Material Proportions of Similar Models. The morphology of the joints has substantial influences for failure modes and mechanical properties [30, 31]. Therefore, investigating the morphological factors that significantly influence shear behavior is increasingly important. The direct shear test is destructive, and natural rock mass cannot carry out the repeated test. Consequently, the jointed cast samples by similar materials were designed to research the effect of morphological factors on shear behavior.

Red sandstone is mainly composed of small solid particles [32]. The ratio and type of similar material are key factors influencing mechanic property of similar models [33, 34]. The brittleness and dilatancy of granular materials can realistically simulate the mechanic property of brittle rocks. The main mineral composition of red sandstone is quartz (SiO_2), according to the XRD results. Granular quartz sand and P.C42.5 cement were selected as aggregate and cementation materials. Silica fume was used to adjust the strength and microstructure, water-reducing agent and defoamer were added to improve the quality and compactness, and iron oxide red was mixed to regulate the color of the similar models. Mechanical parameters of cast jointed samples must be kept following that of natural rock to the maximum after adjusting the proportion of similar materials [33]. The whole test progress is shown in Figure 5.

Through experimental results for similar samples with different similar proportions, as shown in Table 1.

The other specific experimental data will not go into much detail here. The direct shear test results of red sandstone and similar samples are shown in Table 2.

2.3. Preparation Progress of Similar Jointed Models. A test scheme for mechanic properties of the single-jointed similar model was formulated. The joint samples were made with the proportion mentioned in the last section, and the preparation progress is shown in Figure 7.

2.4. Test Schemes. The σ_n (0.1, 2.5, 5.0, 7.5, 10.0, and 12.5 MPa) was kept constant and recording during testing, i.e., CNL was selected in this study. The lower shear block was settled horizontally and movable in vertical. And the shear stress was applied with a loading rate of 0.2 min/mm. Since we need to obtain the joint surfaces in the next shear progresses. The test was carried out with $u = 2.5$ mm; then, the experiment was ended, and the 3D point cloud data of the joints were obtained by VR-5000. The tests were conducted with five kinds of u (2.5, 5.0, 7.5, 10.0, and 12.5 mm), and the corresponding 3D point cloud data were obtained. The shear stress–shear displacement curves of joint samples were obtained and shown in Figure 8. The shear strength decreases to a constant value for all joint samples with u increasing.

3. The 3D Morphology of the Joint Surface

3.1. Roughness of the Joint Surface

3.1.1. Roughness Parameters. The joint surface is composed of complex shapes with various high peaks or depth valleys (Figure 7). The joint surface is anisotropic in view of variable peaks or valleys of each joint. And the mechanic properties are affected by the joints' roughness. Therefore, it is significant to study the roughness parameters of joint surfaces. Four roughness parameters were calculated and compared in the study.

S_d is the ratio between the development area and cross-sectional area of the joint surface:

$$A_i = \iint_{A_{ixy}} \sqrt{1 + z_x^2(x, y) + z_y^2(x, y)}\, dxdy, \tag{1}$$

$$S_d = \frac{\sum_{i=1}^{n} A_i}{A}, \tag{2}$$

where A_i is the i^{th} calculated area, A_{ixy} is the projected area of A_i on the $z = 0$ plane, A is the joint's cross-sectional area, and

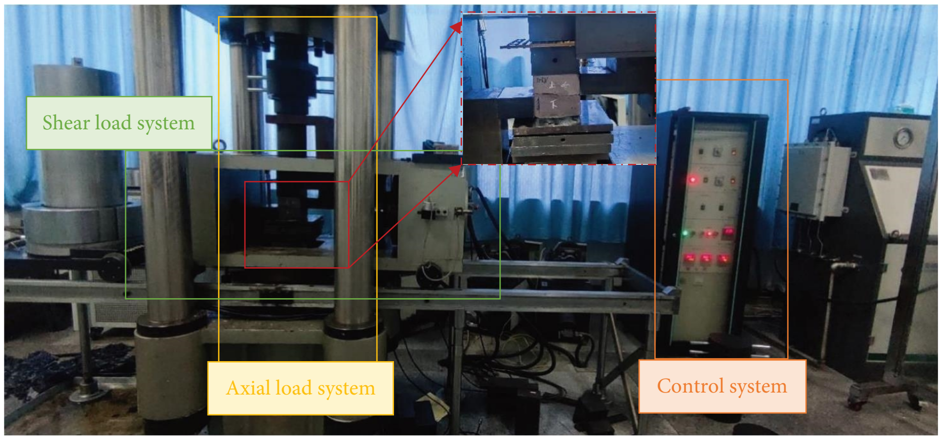

Figure 3: Loading test device.

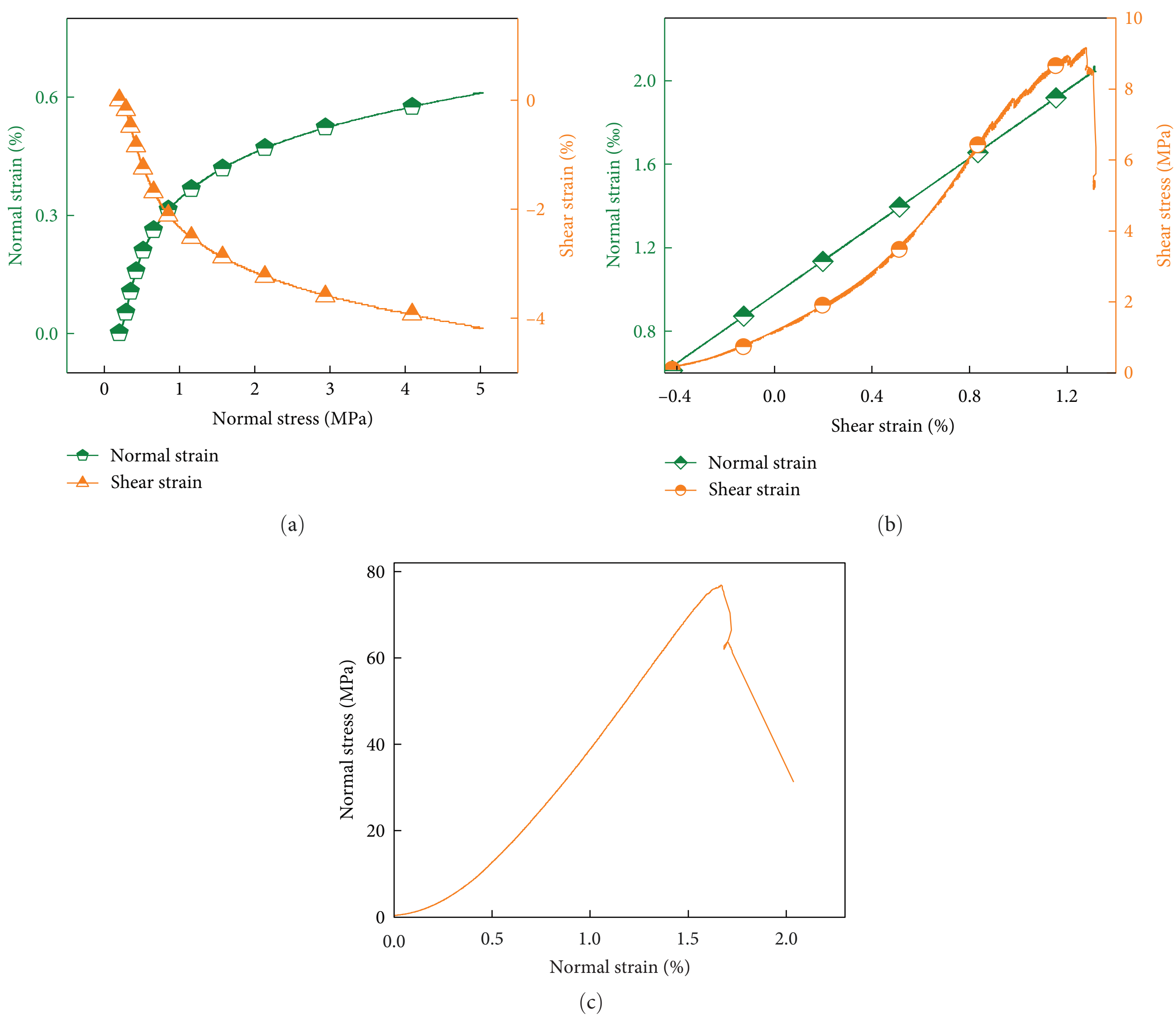

Figure 4: Test results of the red sandstone sample: (a) loading stage of normal stress for the shear test; (b) loading stage of shear stress for the shear test; and (c) uniaxial compression.

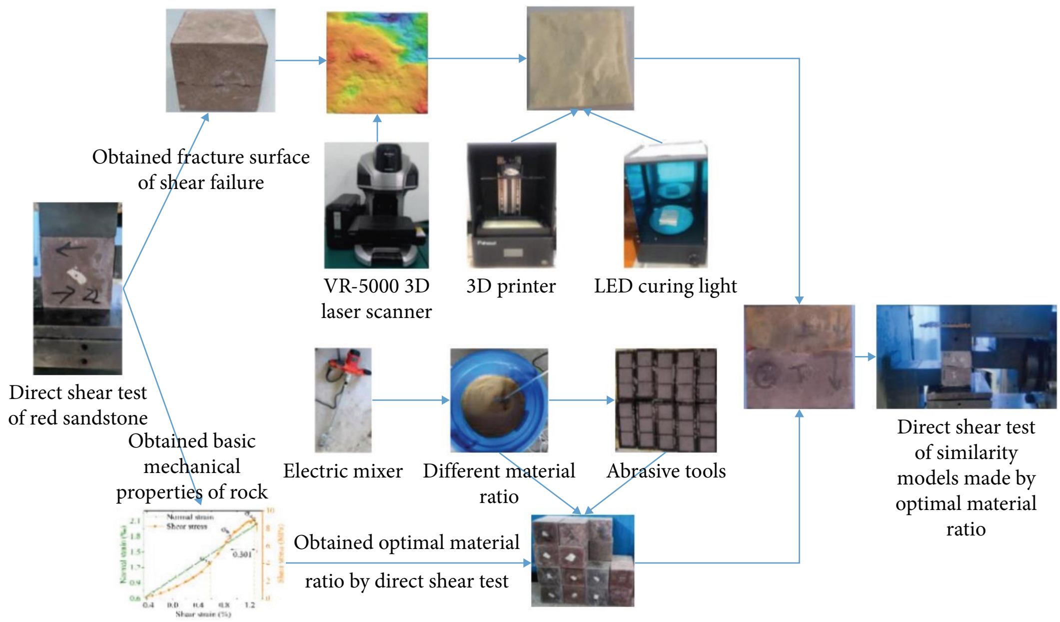

Figure 5: Specific production progress of similar jointed models.

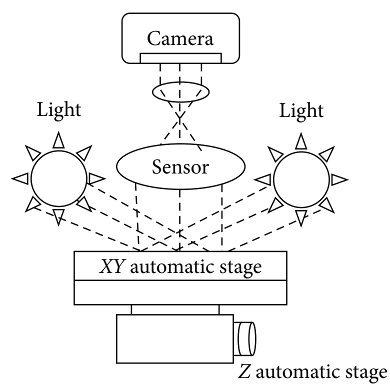

Figure 6: Imaging principle of VR-5000.

Table 1: Mass rate of the similar materials to cement.

Material (%)	Water	Sand	Silica fume	Iron oxide red	Water-reducing agent	Defoamer
Mass rate	55	100	40	3	1	0.1

Table 2: Results of red sandstone and similar samples under direct shear test.

Samples	σ_n (MPa)	τ_n (MPa)	γ_n	G (GPa)
Sandstone	5.0	10.12	1.83	10.31
Model-1	5.0	10.10	1.61	10.38
Model-2	5.0	10.00	1.44	10.26

n is the number of all elements. The surface is entirely flat as $S_d = 1$, and S_d increases with surface wave increasing.

S_{xp} is the ultimate height of peaks ($h_{2.5\%} - h_{50\%}$), that is, the height difference between the average surface and peak after removing particularly high peak, as shown in Figure 9(a). The load curve of the joint surface is a height curve representing the load area ratio $S_{mr(c)}$ from 0% to 100%. And $S_{mr(c)}$ is the ratio of the area above height c to the cross-sectional area of joint surface, as shown in Figure 9(b).

V_{mp} is the volume of the peaks when the load area ratio $S_{mr(c)}$ is 10%, which is expressed as the volume of the peaks at the initial wear stage, as shown in Figure 9(c).

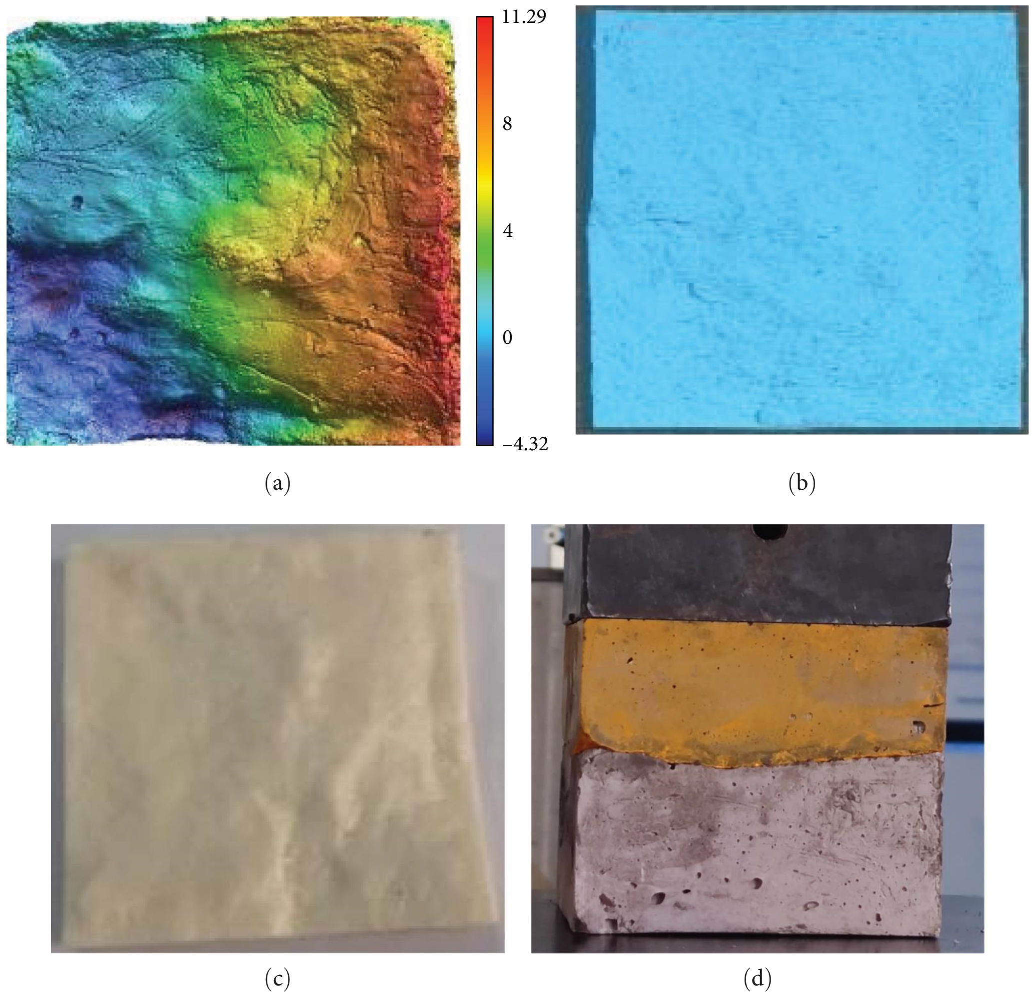

Figure 7: Preparation progress: (a) obtained the 3D point cloud data; (b) built a 3D joint model; (c) print a physical model with a 3D printer; and (d) made samples by the 3D physical model with the materials mentioned.

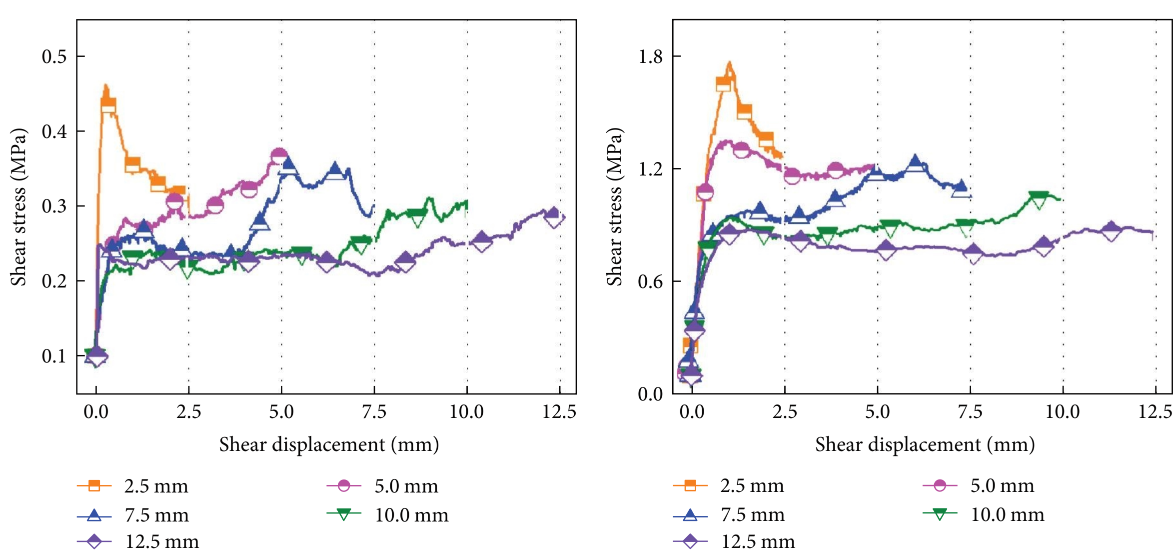

(a) (b)

Figure 8: Continued.

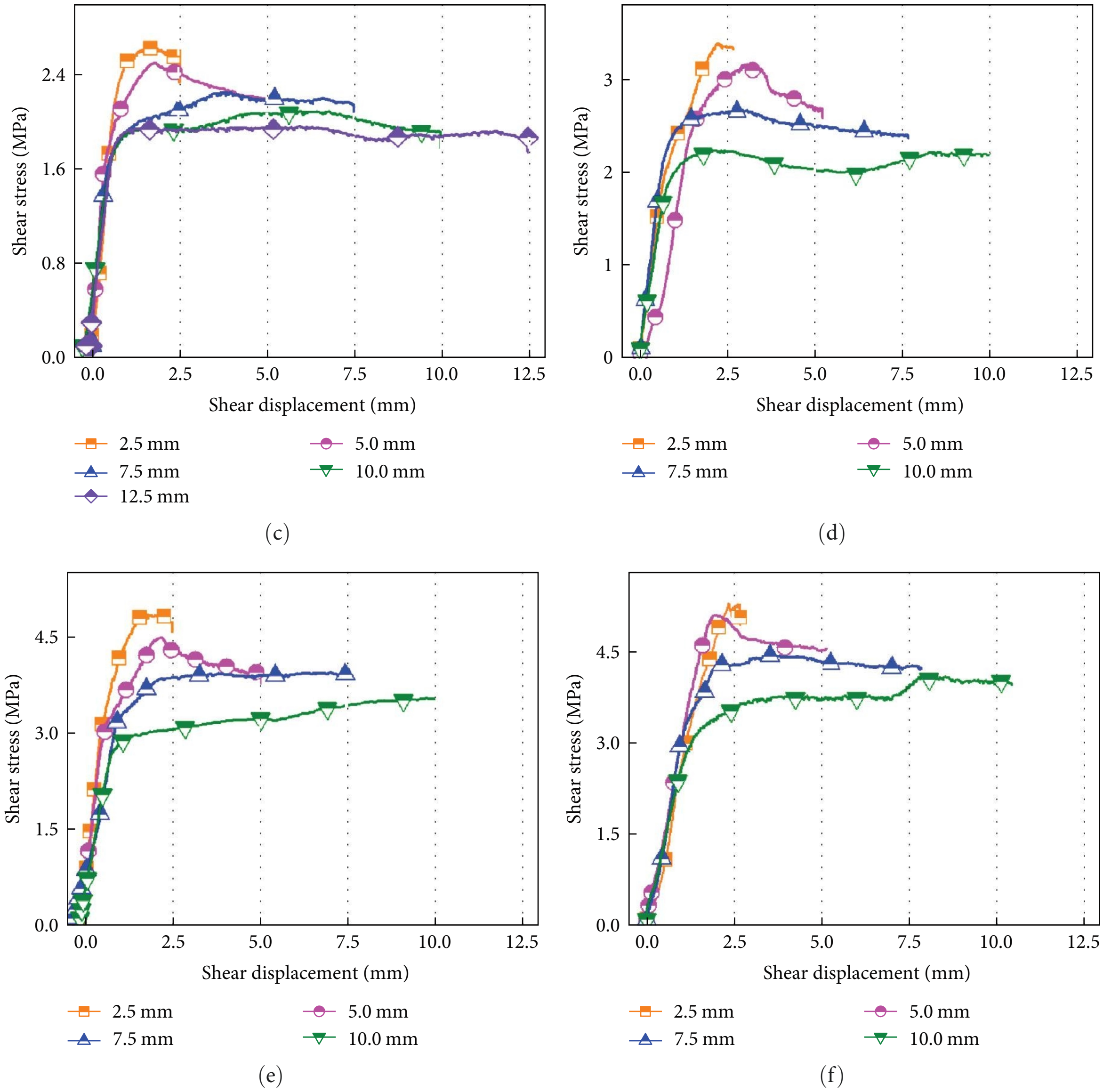

Figure 8: Stress–strain curves of rough joint surfaces under different normal stress: (a) 0.1 MPa; (b) 2.5 MPa; (c) 5.0 MPa; (d) 7.5 MPa; (e) 10.0 MPa; and (f) 12.5 MPa.

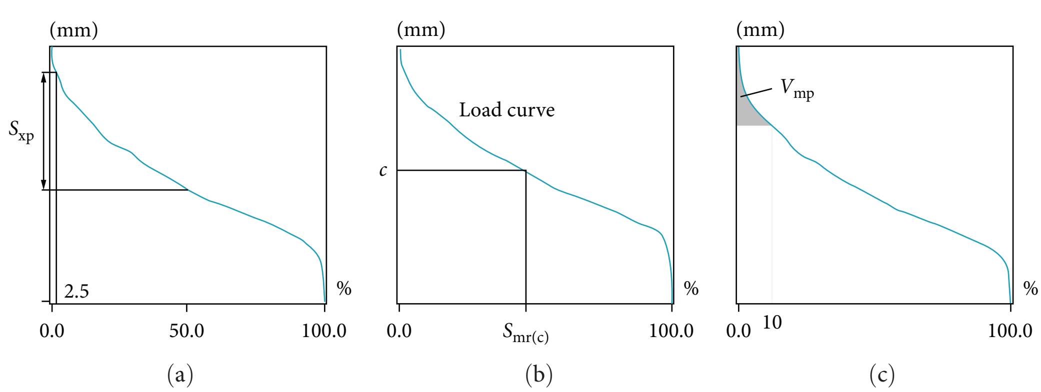

Figure 9: (a) Ultimate height of peaks; (b) load area ratio; and (c) volume of the peaks.

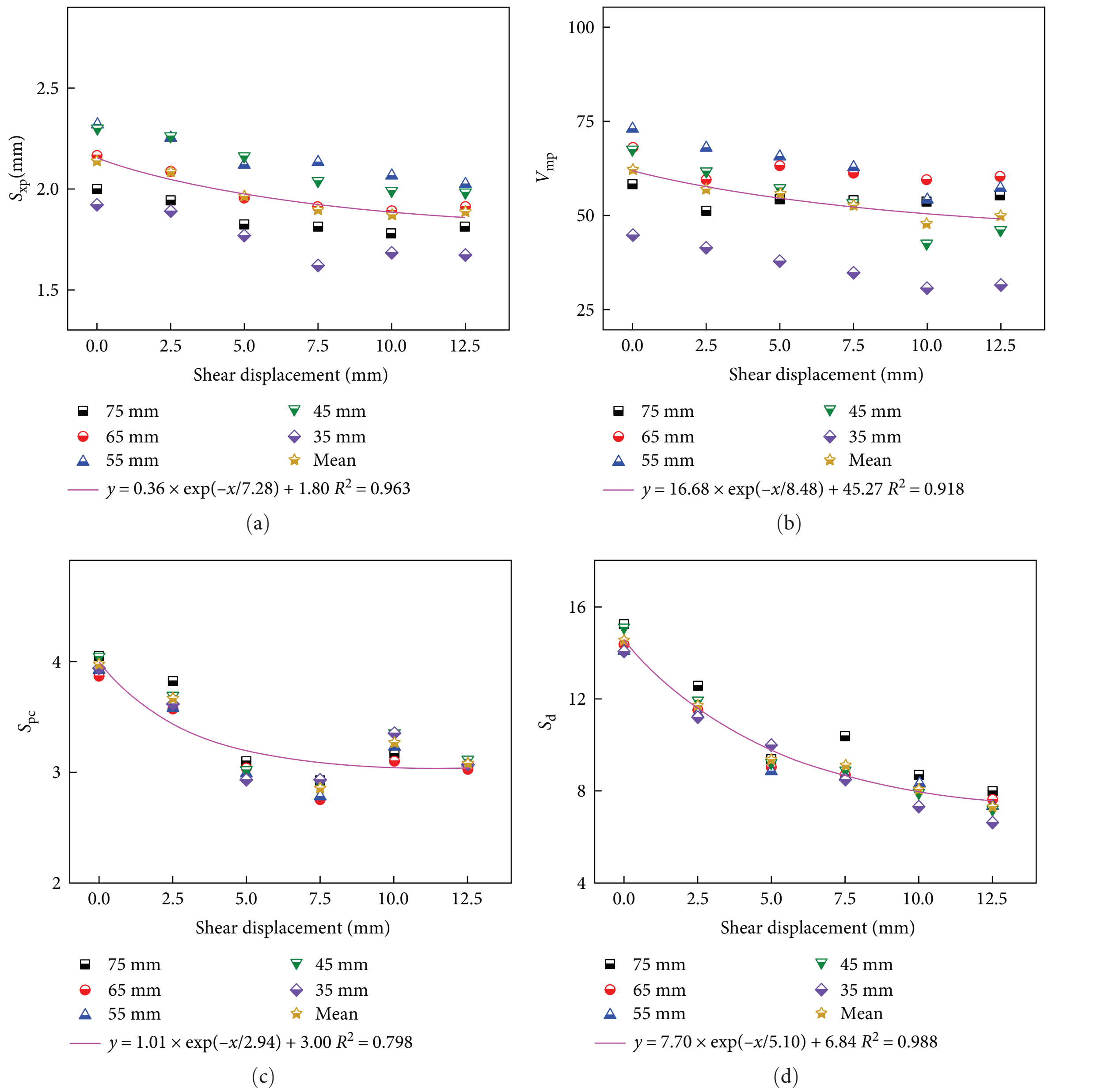

FIGURE 10: Relationship between the four roughness parameters and shear displacement under different analysis dimensions: (a) S_{xp}; (b) V_{mp}; (c) S_{pc}; and (d) S_d.

S_{pc} is the arithmetic mean curvature, representing the mean value of the peaks' vertex curvature. It indicates that the contact point with other objects is circular with a small S_{pc}, and the contact point with other objects is sharp with a large S_{pc}. It can be expressed as:

$$S_{pc} = -\frac{1}{2n}\sum_{k=1}^{n}\left(\frac{\partial^2 z(x,y)}{\partial x^2} + \frac{\partial^2 z(x,y)}{\partial y^2}\right). \quad (3)$$

3.1.2. Evolution of Roughness Parameters. The relationship between the four parameters and shear displacement under different analysis dimensions are shown in Figure 10. It can be concluded that the roughness parameters S_{xp} and V_{mp} are influenced by the analysis size, the roughness parameters S_d and S_{pc} are less influenced by the analysis size. The asperities' height, volume, and curvature; and joint's development area decrease to constant values with u increasing.

3.2. Damage Evolution. The joint's damaged area gradually increases, some asperities of the joint surface were sheared or worn, and white damage areas appeared, as shown in Figure 11. Therefore, we suggest the damage ratio express the damage degree of the joint surfaces, expressed as:

$$d = \frac{A_0}{A}, \quad (4)$$

where d is the damaged ratio, A_0 is the damaged area, and A is the total project of the joint surface.

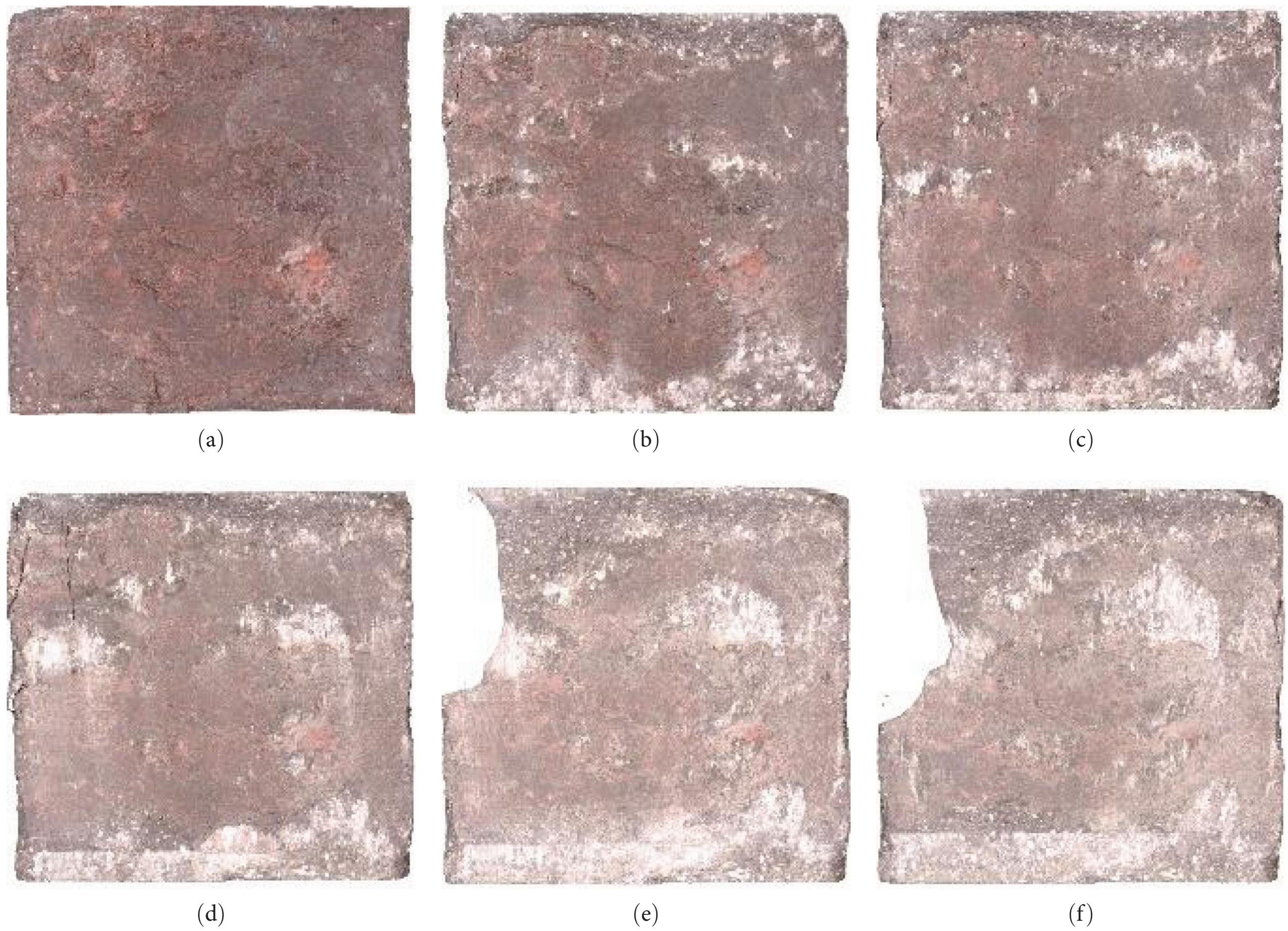

Figure 11: Morphological characteristics of the joint surface under different u: (a) 0 mm; (b) 2.5 mm; (c) 5.0 mm; (d) 7.5 mm; (e) 10.0 mm; and (f) 12.5 mm.

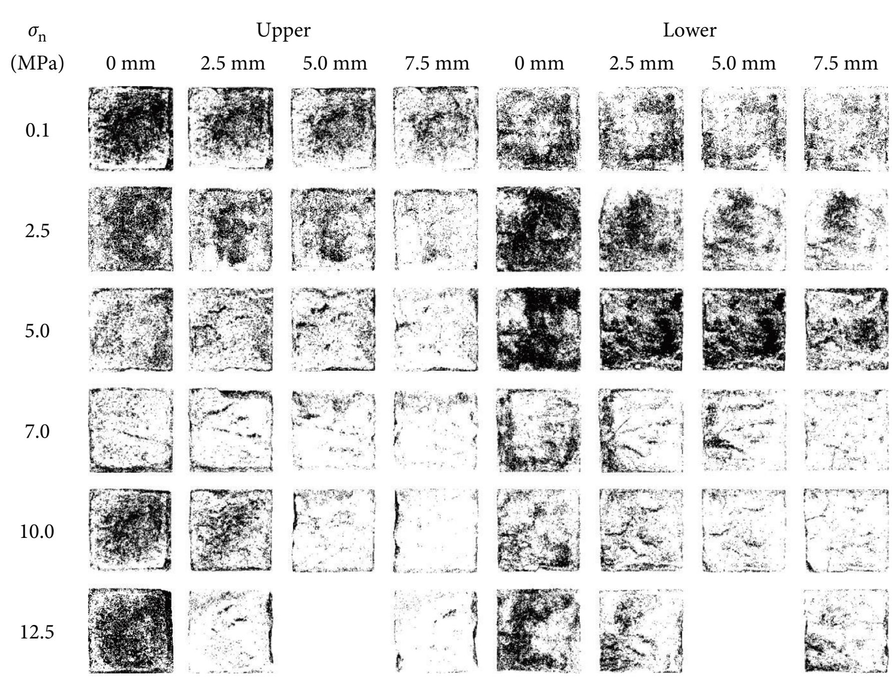

Figure 12: Binarizing the image of the joint surfaces under different σ_n and u.

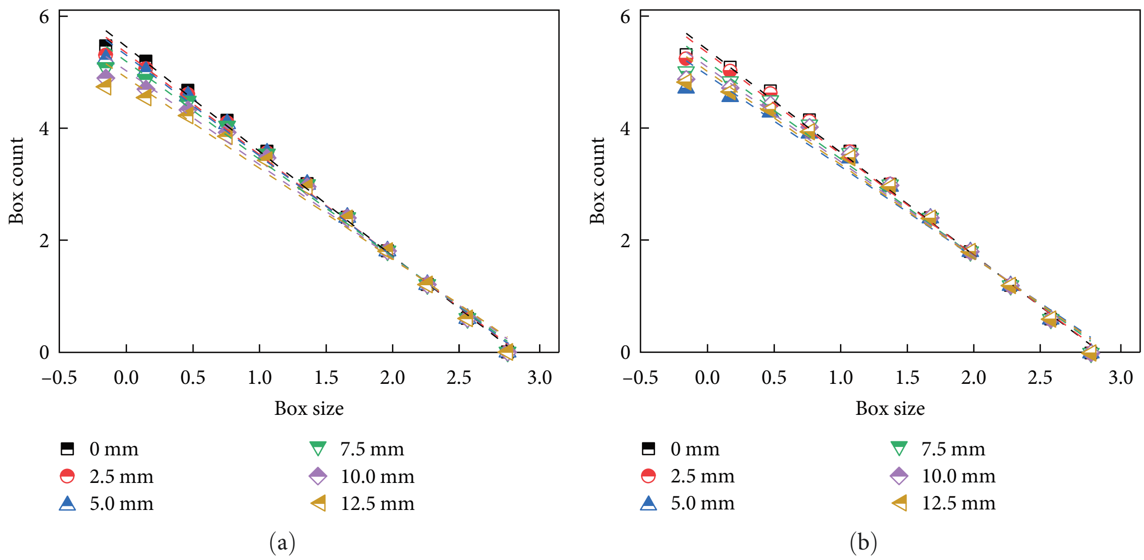

Figure 13: Box-counting dimension [36]: (a) upper surfaces and (b) lower surfaces.

Table 3: Box-counting dimension for upper and lower surfaces.

u (mm)	Upper surfaces		Lower surfaces	
	Expression	R^2	Expression	R^2
0	$\lg N = -1.871 \lg S + 5.451$	0.996	$\lg N = -1.836 \lg S + 5.410$	0.992
2.5	$\lg N = -1.820 \lg S + 5.342$	0.993	$\lg N = -1.811 \lg S + 5.354$	0.991
5.0	$\lg N = -1.800 \lg S + 5.299$	0.992	$\lg N = -1.758 \lg S + 4.953$	0.979
7.5	$\lg N = -1.749 \lg S + 5.190$	0.989	$\lg N = -1.738 \lg S + 5.196$	0.986
10.0	$\lg N = -1.676 \lg S + 5.023$	0.985	$\lg N = -1.694 \lg S + 5.100$	0.982
12.5	$\lg N = -1.621 \lg S + 4.899$	0.981	$\lg N = -1.663 \lg S + 5.023$	0.983

Table 4: Fractal dimension D under different σ_n and u.

u (mm)	σ_n (MPa)											
	Upper surfaces						Lower surfaces					
	0.1	2.5	5.0	7.5	10.0	12.5	0.1	2.5	5.0	7.5	10.0	12.5
0	1.871	1.876	1.785	1.704	1.843	1.894	1.836	1.905	1.901	1.788	1.773	1.846
2.5	1.820	1.815	1.751	1.649	1.798	1.594	1.811	1.841	1.893	1.690	1.733	1.719
5.0	1.800	1.794	1.720	1.570	1.578	—	1.758	1.765	1.823	1.661	1.590	—
7.5	1.749	1.641	1.597	1.526	1.479	1.468	1.738	1.709	1.815	1.536	1.551	1.671
10.0	1.676	1.605	1.524	1.513	1.484	—	1.694	1.631	1.599	—	—	—
12.5	1.621	1.569	—	—	—	—	1.663	1.545	—	—	—	—

The damaged area can be extracted by binarizing joint's image under different σ_n and u, as shown in Figure 12.

As a further test of the damage degree of joint specimens, the fractal theory was selected to process the binary image to express the damage feature quantitatively. The failure area can be characterized by fractal dimensions [35], which can be expressed as:

$$D = \lim_{\varepsilon \to 0} \frac{logN(A, \varepsilon)}{log(1/\varepsilon)}, \tag{5}$$

where A is a nonempty bounded subset of Euclidean space R^n and (A, ε) is the minimum amount of boxes with edge length ε covering A.

Variations of logarithm of box-counting against box size under 0.1 MPa with different u are shown in Figure 13 and Table 3, and the correlation coefficient R^2 is 0.979–0.996.

And the fractal dimension D was obtained by Equation 5, as shown in Table 4.

According to Equations 4 and 5, the d can be expressed by the box dimension of the joint surfaces as:

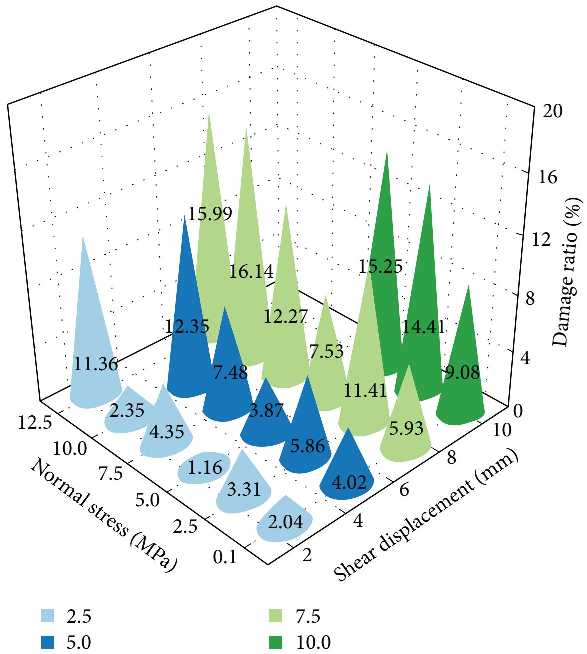

FIGURE 14: Relationship between normal stress on damage ratio under different shear displacements.

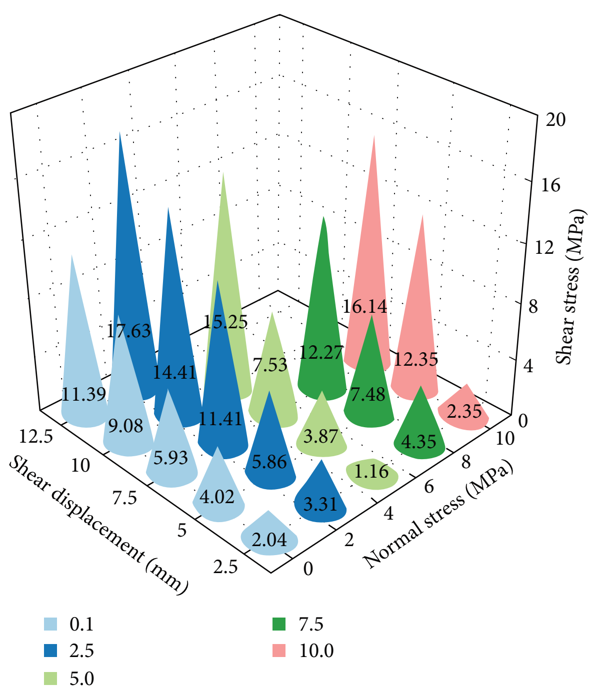

FIGURE 15: Relationship between shear displacement on damage ratio under different normal stress.

$$d = \frac{D_0 - D_i}{D_0}, \tag{6}$$

where D_0 is the box dimension before test and D_i is the box dimension with corresponding displacement.

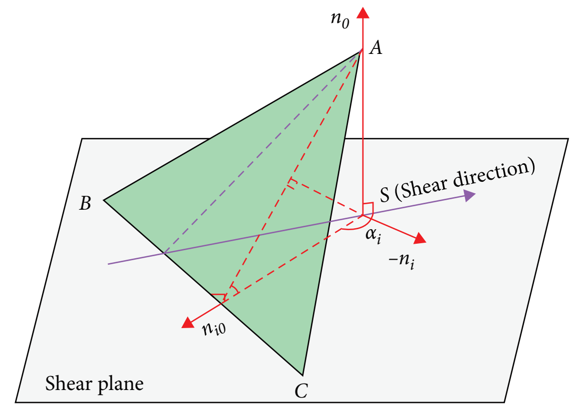

FIGURE 16: Apparent dip angle θ^*, measured along the shear direction concerning the shear plane.

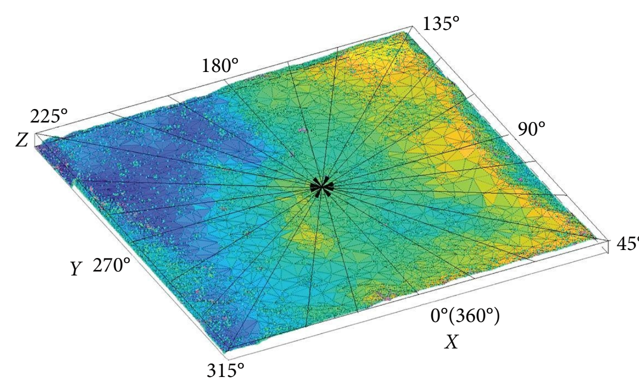

FIGURE 17: Delaunay triangulation of the point cloud data and schematic diagram of the shear directions for joint surfaces.

3.2.1. Influence of Normal Stress on Damage Ratio. The influence of σ_n on damage ratio under different u is shown in Figure 14, and we can find that the joint's damage extent increases with σ_n under the same displacements. The shear strength of joint sample is mainly impacted by rock's basic parameters and joints' morphological parameters [12]. The shear-resisting force provided by sheared asperities with the same joint morphology was determined by rock's basic properties. Meanwhile, the shear strength is influenced by joint's morphology. The area and number of contacted asperities of joints during shearing increase gradually with σ_n. That is, the joint samples' damage ratio increases with σ_n.

3.2.2. Influence of Shear Displacement on Damage Ratio. Not all joint surface areas were involved during shearing, and the shear and wear areas increased significantly with u. The values on damage ratio under different σ_n and u are shown in Figure 15, and there is a positive correlation between u and damage ratio. The joint's damage degree increases with u under the same σ_n. Therefore, it can be inferred that the joint's roughness influenced the shearing resistance provided by the various asperities.

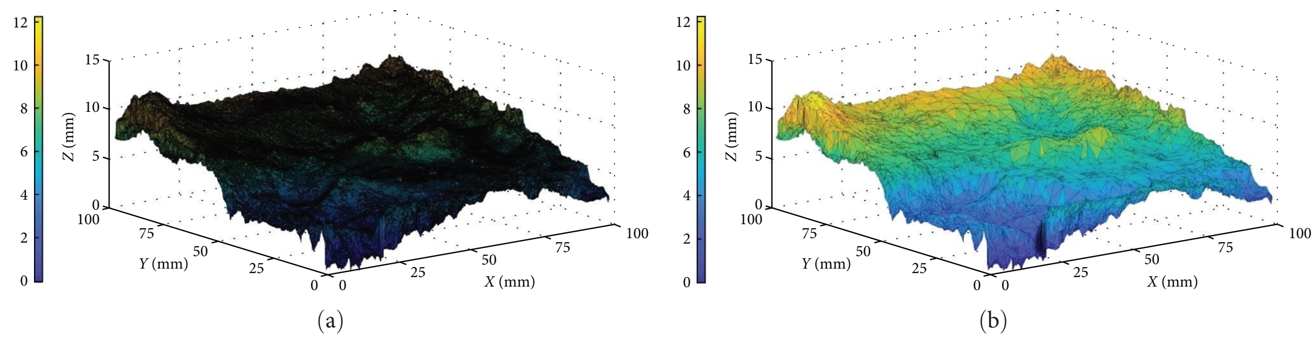

FIGURE 18: Three-dimensional geometrical mode of simulating joint surface with different sampling intervals. (a) S_d and (b) 1.25% S_d.

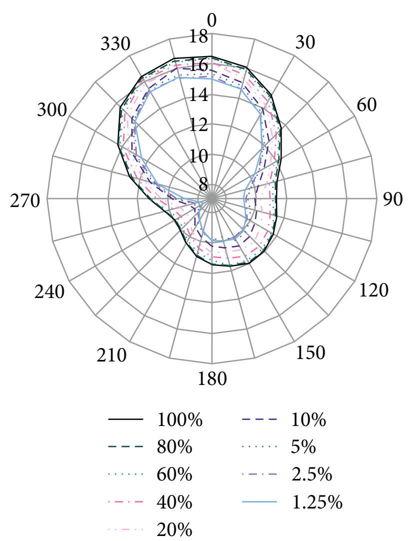

FIGURE 19: Rose plot of the roughness parameter $\theta^*_{max}/(C+1)$ for different shear directions and sampling intervals.

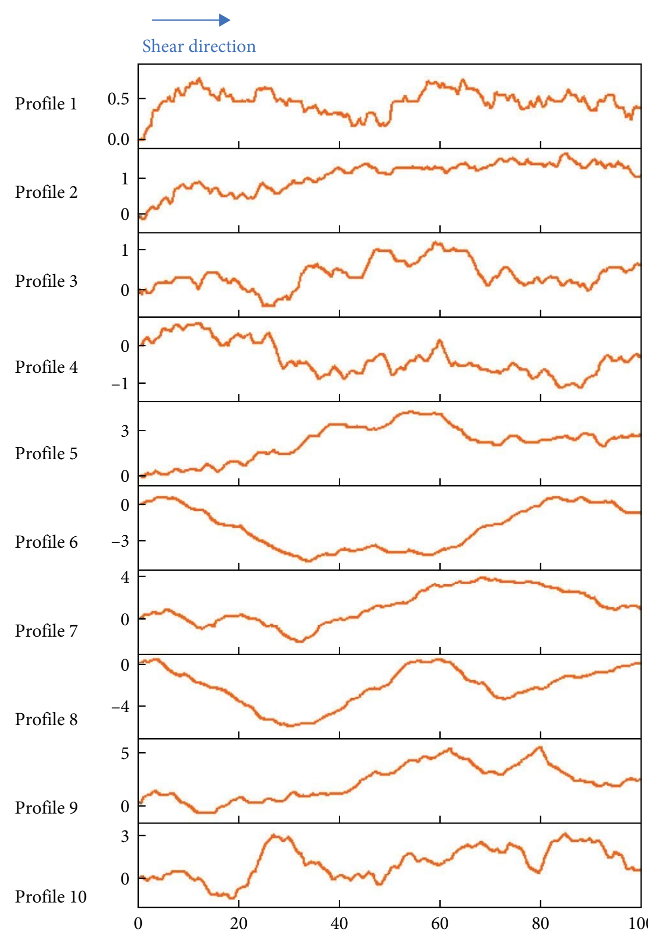

FIGURE 20: Barton's models of 10 typical profiles.

4. Modeling of Postpeak Shear Behavior of Rock Joints

4.1. Postpeak Shear Behavior Modeling Using JRC. The shear stress after peak shear strength decreases and approaches constant values with u increasing, as shown in Figure 8. More asperities were sheared or worn with u increasing exponentially (Figures 10 and 15). These phenomena again demonstrate that the shear strength characteristics were found to have a direct relationship with the joint degradation process during shear [5]. Then the shear stress condition moves into a residual stage, with the roughness weakening into a constant value. Therefore, the *JRC* degradation model of the joint surface can be regarded as:

$$JRC_s = JRC(s) = A\exp\left(-\frac{s}{B}\right) - A + JRC_0, \quad (7)$$

where JRC_0 is the initial roughness, s is the u after the peak shear strength, A and B are the roughness coefficients, and JRC_s is the joint's roughness ($JRC_{s=0} = JRC_0$).

To investigate the influence of joint morphology on shear strength (τ_c), *JRC–JCS* model was proposed [37].

$$\tau_c = \sigma_n \tan\left[JRC \cdot log_{10}\left(\frac{JCS}{\sigma_n}\right) + \varphi_b\right], \quad (8)$$

where φ_b is the friction angle of plane joint and *JCS* is the compressive strength.

The shear stress of the joint samples after the peak shear strength is related to joint's roughness at a certain s. Therefore, the postpeak stress of the joint rock can be expressed as:

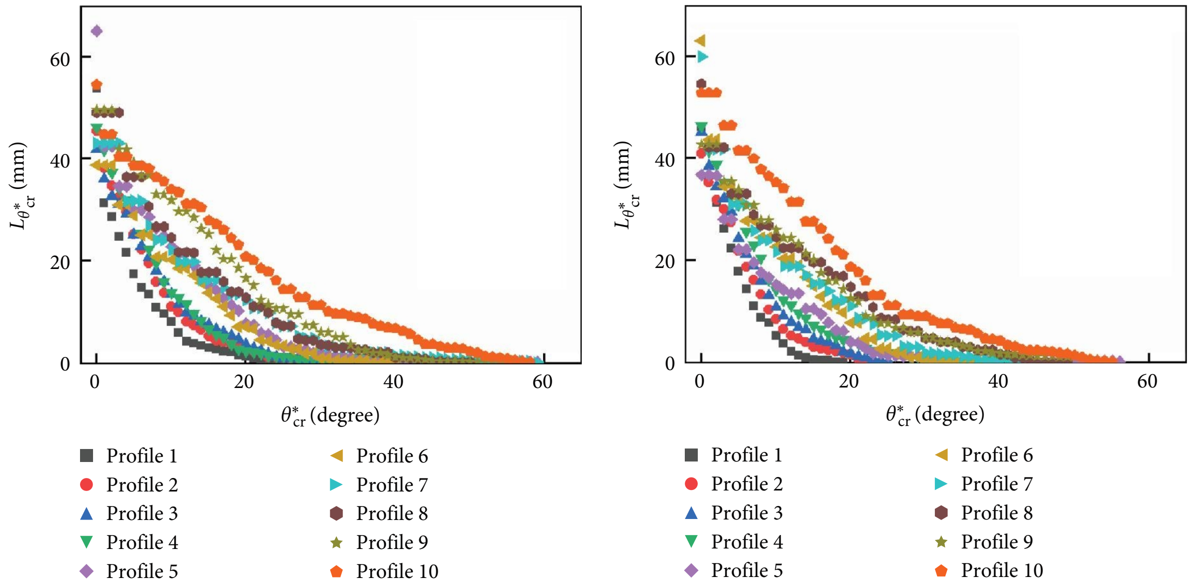

(a) (b)

FIGURE 21: Projected contact length under different apparent dip angle thresholds of Barton's 10 typical profiles: (a) direction I and (b) direction II.

$$\tau_s = \sigma_n \tan\left[JRC_s \cdot log_{10}\left(\frac{JCS}{\sigma_n}\right) + \varphi_b\right] = \sigma_n \tan\left[\left(A\exp\left(-\frac{s}{B}\right) - A + JRC_0\right) \cdot log_{10}\left(\frac{JCS}{\sigma_n}\right) + \varphi_b\right], \tag{9}$$

where τ_s is the postpeak stress.

4.2. Estimating the JRC of the 3D Joint Surfaces

4.2.1. Estimating Method. Grasselli et al. [38] proposed a method to estimate the 3D joint's roughness for solving the variability of the potential contact area (A_{θ^*}) and apparent dip angle (θ^*). $\theta^*_{max}/(C+1)$ was used as the roughness parameter which has proved a positive correlation with the contact area [6].

$$A_{\theta^*} = A_0\left(\frac{\theta^*_{max} - \theta^*_{cr}}{\theta^*_{max}}\right)^C, \tag{10}$$

where θ^* is the apparent dip angle, θ^*_{cr} is the threshold of θ^*, A_{θ^*} is the total area of the potential contact microelements, A_0 is the total area of the microelements as $\theta^*_{cr} = 0$, C is the joint's roughness coefficient, and θ^*_{max} is the maximum θ^* along the shear direction.

The microelement is just in contact as $\theta^* = \theta^*_{cr}$, deformed or crushed as $\theta^* > \theta^*_{cr}$, and uncontacted as $\theta^* < \theta^*_{cr}$. The apparent dip angle θ^* can be expressed as Equation 11 (Figure 16).

$$\tan\theta^* = -\cos\alpha\tan\theta, \tag{11}$$

where α is the angle between the microelement and the shear direction, and θ is the angle between the microelement and the shear plane.

$$\cos\alpha = \frac{\boldsymbol{s}\boldsymbol{n}_{i0}}{|\boldsymbol{s}||\boldsymbol{n}_{i0}|}, \tag{12}$$

where $\boldsymbol{s}$ is the shear vector, $\boldsymbol{n}_i$ is the normal vector of microelement, and $\boldsymbol{n}_{i0}$ is the projection vector of the $\boldsymbol{n}_i$ in the shear plane.

$$cos\theta = \frac{\boldsymbol{n}_0\boldsymbol{n}_{i0}}{|\boldsymbol{n}_0||\boldsymbol{n}_{i0}|}, \tag{13}$$

where $\boldsymbol{n}_0$ is the normal vector of the shear plane.

The approach is worked out as follows:

(1) Collect and process 3D joint surface information. The joint's 3D point cloud data were got by VR-5000 which were expressed as a matrix N. The matrix N is with three rows corresponding the 3D coordinates of the discrete points. And the rows' number in matrix N is the discrete points' number.
(2) Establish the joint's 3D geometric modeling. The Delaunay triangulation algorithm has the uniqueness of the results. Therefore, it was selected to triangulate the discrete points to establish a 3D model (Figure 17).
(3) Calculate the joint's real contact area based on the directions.
(4) Obtain the roughness parameter, $\theta^*_{max}/(C+1)$.

4.2.2. Effect of Sampling Interval on $\theta^*_{max}/(C+1)$. The value of $\theta^*_{max}/(C+1)$ is related to the shear directions. And they were selected as shown in Figure 17, with 0° (360°) and 90° along the positive direction of the y and x axes, respectively. The calculation is conducted every 15° clockwise in the xy plane.

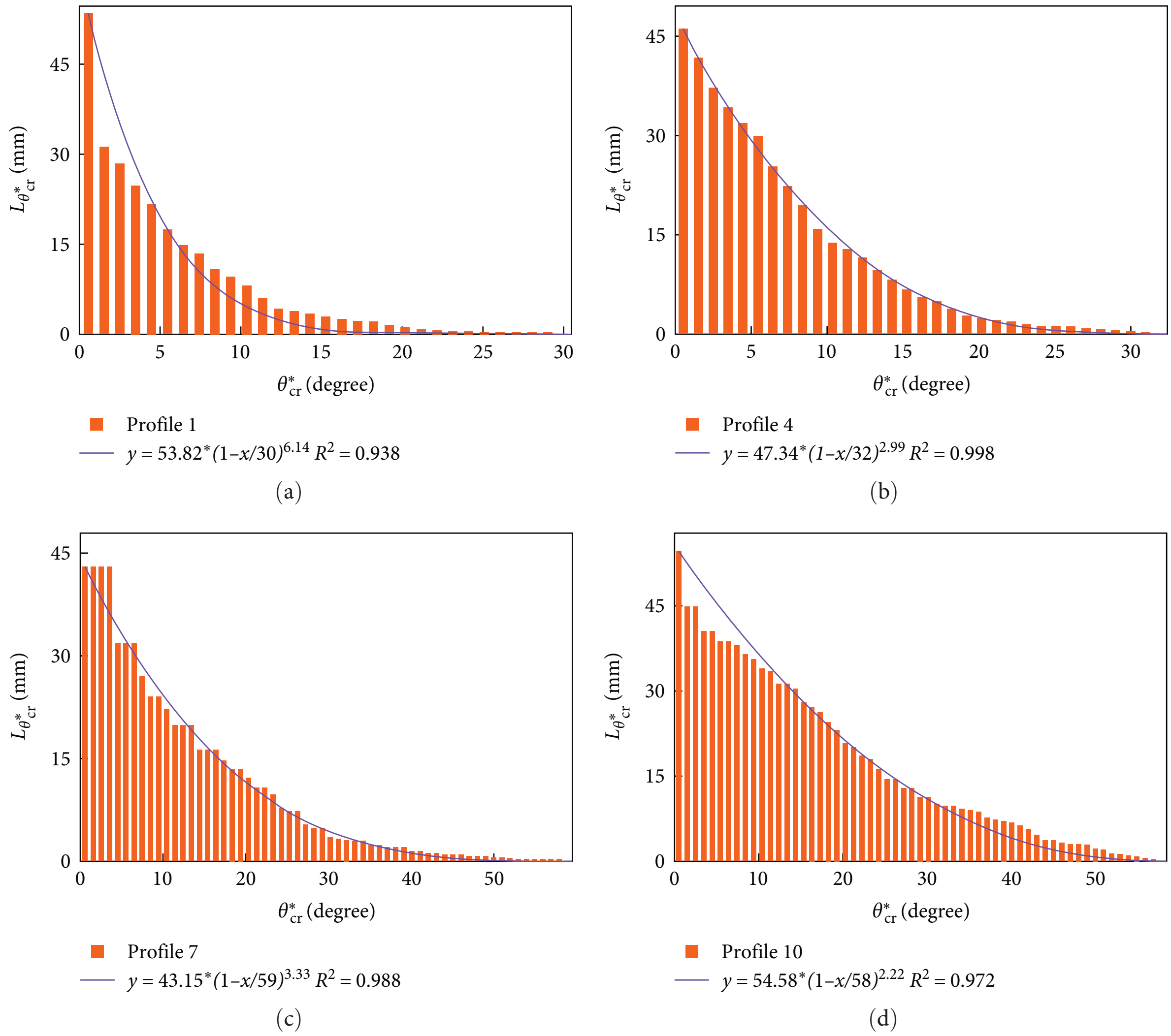

FIGURE 22: Relationship between the projected contact length and apparent dip angle: (a) profile 1; (b) profile 4; (c) profile 7; and (d) profile 10.

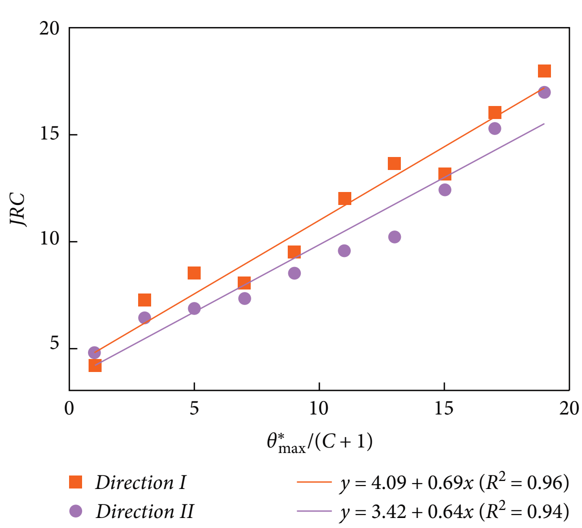

FIGURE 23: The relationship between $\theta^*_{max}/(C+1)$ and JRC.

The joint surface was selected to study the effect of sampling interval on $\theta^*_{max}/(C+1)$ (taking $\sigma_n = 5.0$ MPa with $u = 2.5$ mm as an example, as shown in Figure 18(a). The initial sampling interval is 0.12 mm, and the number of the microelement S_d is 1,339,616. And the joint surfaces with different sampling intervals were produced and obtained by the software SOLIDWORKS, taking 80%, 60%, 40%, 20%, 10%, 5%, 2.5%, and 1.25% of the S_d, respectively (Figure 18(b)).

$\theta^*_{max}/(C+1)$ of the joint with different sampling intervals were obtained under 24 shear directions (Figure 19). The results indicate that the joint's roughness $\theta^*_{max}/(C+1)$ in the same direction declines with increasing sampling interval, consistent with previous research results. The phenomenon is because its precision increases as the spacing between discrete points decreases when establishing a joint surface model. The discrete points with small-sampling intervals can extract more roughness due to the fractal characteristics of the joint surface. Therefore, the estimated roughness

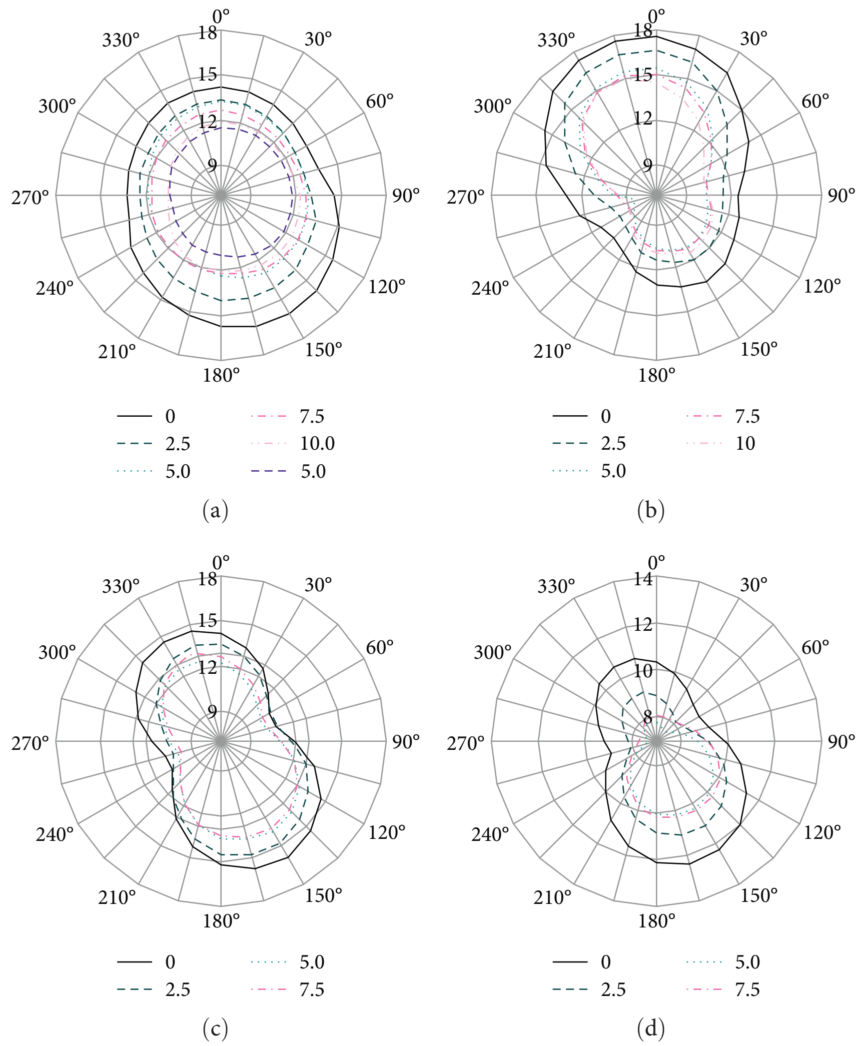

Figure 24: Rose plot of the $\theta^*_{\max}/(C+1)$ for different shear directions and displacements for the joint surfaces: (a) 2.5 MPa; (b) 5.0 MPa; (c) 7.5 MPa; and (d) 10.0 MPa.

Table 5: Relationship between JRC and s under different σ_n.

σ_n (MPa)	Fitting formulas	R^2
2.5	$JRC = 11.71 + 3.26\exp(-0.20s)$	0.965
5.0	$JRC = 11.45 + 1.62\exp(-0.54s)$	0.967
7.5	$JRC = 12.44 + 2.18\exp(-0.14s)$	0.971
10.0	$JRC = 10.96 + 1.51\exp(-0.39s)$	0.979

parameter of the joint surface increases as the sampling interval decreases.

4.2.3. Relationship between $\theta^*_{\max}/(C+1)$ and JRC. The roughness parameter, $\theta^*_{\max}/(C+1)$ is a widely recognized method to evaluate the joint's roughness correctly. Therefore, it is also suitable to estimate the roughness of 2D roughness profiles. The characteristics of $\theta^*_{\max}/(C+1)$ related to the JRC were discussed based on Barton's models of 10 typical profiles (Figure 20). The direction facing the shear direction was noted as direction I, and the direction opposite the shear direction was referred to as direction II.

And the profiles' projected contact length under the different apparent dip angle thresholds was obtained by the method expressed before. The projected contact length of the profiles in and against the shear direction, describing the part that is more steeply inclined than progressively higher θ^*_{cr} (such as 0, 1, 2, …, and $\theta^*_{\max}$), the results are plotted in Figure 21.

And C is a dimensionless fitting parameter; the larger $\theta^*_{\max}/(C+1)$ is, the rougher the joint surface [39]; the part results in direction I are shown in Figure 22.

The relationship between $\theta^*_{\max}/(C+1)$ and JRC of the profiles shown in Figure 20 were studied and obtained, as shown in Figure 23. In the two direction conditions, $\theta^*_{\max}/(C+1)$ increases with the profiles's JRC, and R^2 of the two directions are 0.96 and 0.94, respectively. That is, the value of $\theta^*_{\max}/(C+1)$ is correlated significantly with JRC.

4.3. Verified the Postpeak Shear Behavior Modeling. The four joint surfaces under different σ_n (2.5, 5.0, 7.5, and 10.0 MPa) were further used to analyze the anisotropy and the trend with u of the surface roughness. We calculated $\theta^*_{\max}/(C+1)$

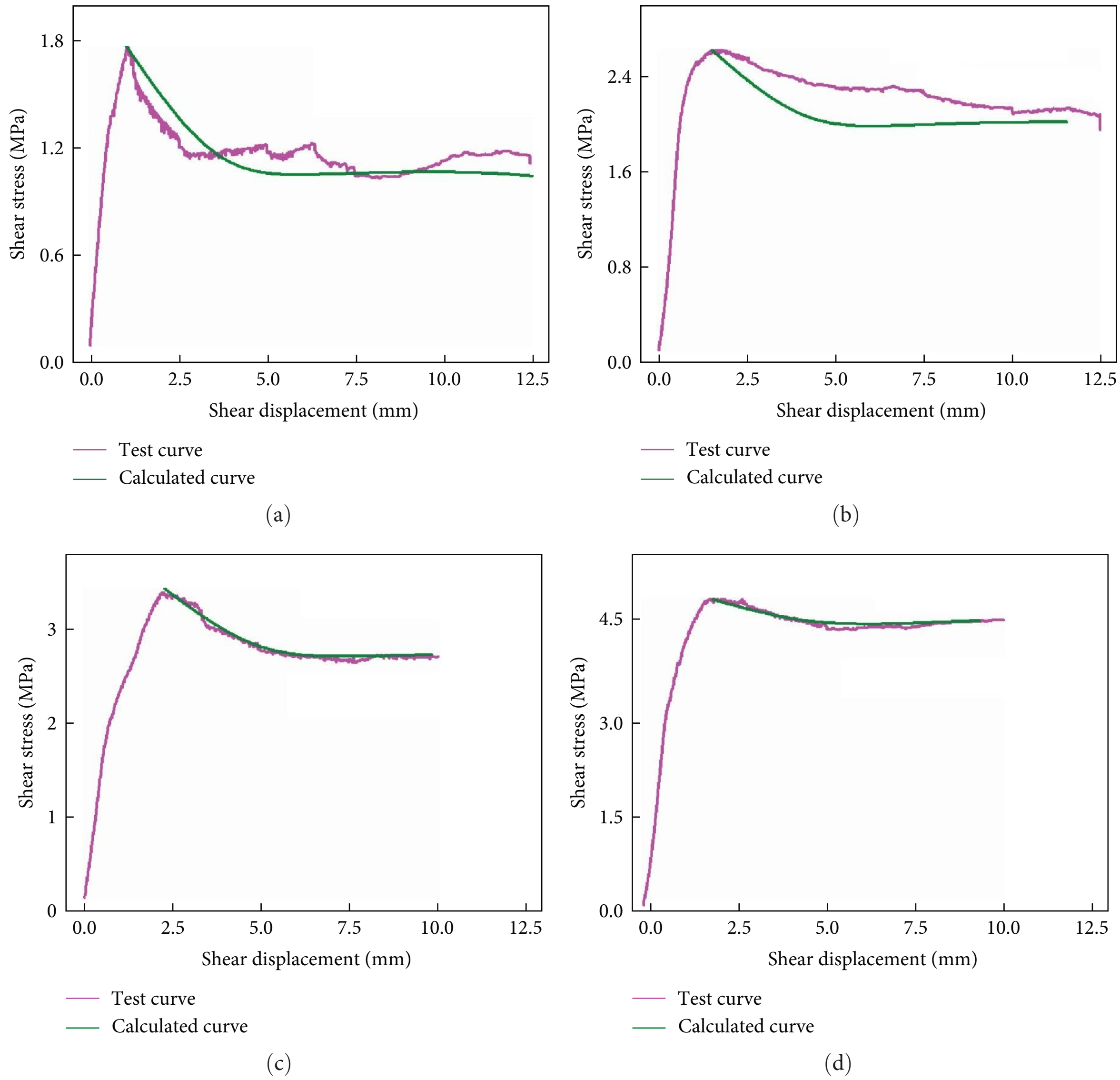

Figure 25: Comparison between the test and the postpeak shear behavior modeling in predicting the stress–displacement curve for joint surface: (a) 2.5 MPa; (b) 5.0 MPa; (c) 7.5 MPa; and (d) 10.0 MPa.

from 24 directions under different σ_n and u, the values corresponding to each situation can be displayed to visualize the joint's anisotropy (Figure 24).

Figure 24 illustrates that the roughness values in various directions show different contour features under different σ_n in rose diagram. The roughness values $\theta^*_{\max}/(C+1)$ with a larger u is smaller than those with a small displacement, which corresponds to the joint's morphological features shown in Figure 11. Further, each joint's roughness can be objectively evaluated based on the size of the contour. To calculate the postpeak shear stress of the test joint surfaces in Equation 9, the JRC of the joint surfaces under different u was calculated according to Equation 7, and the relationship between JRC and s was obtained as shown in Table 5.

The stress–displacement curves resulting from the experiment and proposed modified model are demonstrated in Figure 25. It is proved that the proposed model works well in predicting stress–displacement curve, which can prove the effectiveness of postpeak shear behavior modeling.

5. Conclusions

This study used an experimental method on anisotropic joint surfaces to analyze the damage and roughness evolution under direct shear test conditions to understand better the effect of burial depth, displacement, and joint surface morphology on the shear performance of jointed rock masses. Four roughness parameters and the damaged area quantitatively described by box dimension were obtained to study the roughness evolution of joint surfaces. And a model was proposed based on regression analyses to evaluate the JRC values of rock joints under different loading conditions. Additionally, a new postshear behavior modeling was proposed for rock joints based on surface degradation characteristics under various initial joint roughness coefficients (JRC_0) and normal stress. The joint surfaces with rough morphology were obtained by 3D scanning and printing technology, the joint samples with similar materials were cast, and shear tests were performed under different σ_n and u. The main conclusions of this study are as follows:

The roughness parameters S_{xp} and V_{mp} are influenced by the analysis size, the roughness parameters S_d and S_{pc} are less influenced by the analysis size, and all roughness parameters decrease with u. The height, volume, and curvature of the asperities and the development area of the joint surface decrease with u increasing. In conclusion, the damage degree of the joint surface gradually increases with u.

The damaged ratio was proposed to characterize the damaged degree of the joint surface. The damaged area was quantitatively described with the image binarization and box dimension. And the quantitative extraction of the damaged area was used to obtain the damage ratio of the joint surface. The corresponding statistical analysis of the data from the test shows that the damage ratio of the anisotropic joint decreases with u and σ_n increasing, which weakens the shear strength of rough joints.

The value $\theta^*_{\max}/(C+1)$ of the joint surfaces was obtained, which proved that it increases with the decrease of sampling interval and affected by the shear direction. And the relationship between the JRC and $\theta^*_{\max}/(C+1)$ based on Barton's models of 10 typical profiles. Then, JRC was estimated by $\theta^*_{\max}/(C+1)$ of the 3D joint surface.

An equation of the JRC_s degradation model was proposed to predict the JRC values of rock joints under different s, which considered the impact factors of JRC_0 and s. Then, a new mechanical model of postpeak shear stress was proposed according to the JRC_s degradation model. The stress–displacement curves resulting from the proposed modified model work well in the test postpeak stress–displacement curve, which proves the effectiveness of the postpeak shear behavior modeling.

The future focus and difficulty in further studies lie in applying this method to the roughness evaluation of 3D joint surface under different sampling intervals, and the anisotropy of joint roughness will be focused.

Data Availability

Data available on request through the authors (gfeng-cumt@126.com).

Additional Points

Highlights. (1) Investigated four different parameters and the damaged ratio quantitatively described by the image binarization and box dimension to study the roughness evolution of joint surfaces. (2) Presented a JRC degradation model based on regression analyses under various displacements to replace the JRC in the JRC–JCS model. (3) Proposed a mechanical model for postpeak shear behavior of rock joints based on surface degradation characteristics under various JRC_0 and normal stress.

Conflicts of Interest

The authors declare that they have no conflicts of interest.

Acknowledgments

Throughout the writing of this manuscript, I have received a great deal of support and assistance. I would first like to thank Feng Gao, who provided experimental ideas. I would like to acknowledge Yan Xing for her support in the experiment. This work was financially supported by the National Natural Science Foundation of China (Nos. 51934007, 51604263, and 52004268).

References

[1] X. Zhang, Q. Jiang, N. Chen, W. Wei, and X. Feng, "Laboratory investigation on shear behavior of rock joints and a new peak shear strength criterion," *Rock Mechanics and Rock Engineering*, vol. 49, no. 9, pp. 3495–3512, 2016.

[2] Q. Liu, Y. Tian, P. Ji, and H. Ma, "Experimental investigation of the peak shear strength criterion based on three-dimensional surface description," *Rock Mechanics and Rock Engineering*, vol. 51, no. 4, pp. 1005–1025, 2018.

[3] Y. L. Dai, "A damage constitutive model for intermittent jointed rocks under cyclic uniaxial compression," *International Journal of Rock Mechanics and Mining Sciences*, vol. 103, pp. 289–301, 2018.

[4] J. Ma, J. Zhao, Y. Lin et al., "Study on tamped spherical detonation-induced dynamic responses of rock and pmma through mini-chemical explosion tests and a four-dimensional lattice spring model," *Rock Mechanics and Rock Engineering*, vol. 56, no. 10, pp. 7357–7375, 2023.

[5] L. He, Z. Zhao, J. Chen, and D. Liu, "Empirical shear strength criterion for rock joints based on joint surface degradation characteristics during shearing," *Rock Mechanics and Rock Engineering*, vol. 53, no. 8, pp. 3609–3624, 2020.

[6] C.-C. Xia, Z.-C. Tang, W.-M. Xiao, and Y.-L. Song, "New peak shear strength criterion of rock joints based on quantified surface description," *Rock Mechanics and Rock Engineering*, vol. 47, no. 2, pp. 387–400, 2014.

[7] J. N. Otoo, N. H. Maerz, X. Li, and Y. Duan, "Verification of a 3-D LiDAR viewer for discontinuity orientations'," *Rock Mechanics and Rock Engineering*, vol. 46, no. 3, pp. 543–554, 2013.

[8] H. T. Nguyen, T. M. Fernandez-Steeger, T. Wiatr, D. Rodrigues, and R. Azzam, "Use of terrestrial laser scanning for engineering geological applications on volcanic rock slopes—an example from Madeira island (Portugal)," *Natural Hazards and Earth System Sciences*, vol. 11, no. 3, pp. 807–817, 2011.

[9] T. Drews, G. Miernik, K. Anders et al., "Validation of fracture data recognition in rock masses by automated plane detection in 3D point clouds," *International Journal of Rock Mechanics and Mining Sciences*, vol. 109, pp. 19–31, 2018.

[10] K. Kishida, Y. Kawaguchi, S. Nakashima, and H. Yasuhara, "Estimation of shear strength recovery and permeability of single rock fractures in shear-hold-shear type direct shear tests," *International Journal of Rock Mechanics and Mining Sciences*, vol. 48, no. 5, pp. 782–793, 2011.

[11] H. S. Lee, Y. J. Park, T. F. Cho, and K. H. You, "Influence of asperity degradation on the mechanical behavior of rough rock joints under cyclic shear loading," *International Journal of Rock Mechanics and Mining Sciences*, vol. 38, no. 7, pp. 967–980, 2001.

[12] Q. Jiang, L. Song, F. Yan, C. Liu, B. Yang, and J. Xiong, “Experimental investigation of anisotropic wear damage for natural joints under direct shearing test,” *American Society of Civil Engineers*, vol. 20, no. 4, Article ID 04020015, 2020.
[13] L. Wang, Y. Xue, Z. Cao, H. Kong, J. Han, and Z. Zhang, “Experimental study on mode I fracture characteristics of granite after low temperature cooling with liquid nitrogen,” *Water*, vol. 15, no. 19, Article ID 3442, 2023.
[14] Y. Li, W. Wu, C. Tang, and B. Liu, “Predicting the shear characteristics of rock joints with asperity degradation and debris backfilling under cyclic loading conditions,” *International Journal of Rock Mechanics and Mining Sciences*, vol. 120, pp. 108–118, 2019.
[15] L. Ban, W. Du, and C. Qi, “’Stability analysis of anchored slopes based on a peak shear-strength criterion of rock joints’,” *Environmental Earth Sciences*, vol. 79, no. 10, 2020.
[16] D. Casagrande, O. Buzzi, A. Giacomini, C. Lambert, and G. Fenton, “A new stochastic approach to predict peak and residual shear strength of natural rock discontinuities,” *Rock Mechanics and Rock Engineering*, vol. 51, no. 1, pp. 69–99, 2018.
[17] R. Kumar and A. K. Verma, “Corrections applied to direct shear results and development of modified Barton’s shear strength criterion for rock joints,” *Arabian Journal of Geosciences*, vol. 13, Article ID 1019, 2020.
[18] H. Xie, J.-A. Wang, and W.-H. Xie, “Fractal effects of surface roughness on the mechanical behavior of rock joints,” *Chaos, Solitons & Fractals*, vol. 8, no. 2, pp. 221–252, 1997.
[19] N. H. Maerz, J. A. Franklin, and C. P. Bennett, “Joint roughness measurement using shadow profilometry,” *International Journal of Rock Mechanics and Mining Sciences & Geomechanics Abstracts*, vol. 27, no. 5, pp. 329–343, 1990.
[20] Z. Y. Yang, S. C. Lo, and C. C. Di, “Reassessing the joint roughness coefficient (JRC) estimation using $Z_2^{'}$,” *Rock Mechanics and Rock Engineering*, vol. 34, pp. 234–251, 2001.
[21] T. Yang, P. Wang, T. Xu et al., “Anisotropic characteristics of jointed rock mass: a case study at Shirengou iron ore mine in China,” *Tunnelling and Underground Space Technology*, vol. 48, no. 48, pp. 129–139, 2015.
[22] Q. Jiang, B. Yang, F. Yan, C. Liu, Y. Shi, and L. Li, “New method for characterizing the shear damage of natural rock joint based on 3D engraving and 3D scanning,” *International Journal of Geomechanics*, vol. 20, no. 2, Article ID 06019022, 2020.
[23] S. Su, P. Hou, F. Gao et al., “A fractal perspective on structural damage and fracture characteristics of coal subjected to liquid nitrogen cooling at laboratory-scale,” *Fractals—An Interdisciplinary Journal on the Complex Geometry of Nature*, vol. 30, no. 4, 2022.
[24] N. Babanouri and S. K. Nasab, “Modeling spatial structure of rock fracture surfaces before and after shear test: a method for estimating morphology of damaged zones,” *Rock Mechanics and Rock Engineering*, vol. 48, pp. 1051–1065, 2015.
[25] S. J. Chen, W. C. Zhu, Q. L. Yu, and X. G. Liu, “characterization of anisotropy of joint surface roughness and aperture by variogram approach based on digital image processing technique,” *Rock Mechanics and Rock Engineering*, vol. 49, no. 3, pp. 855–876, 2016.
[26] J. Ma, J. Chen, W. Chen, and L. Huang, “A coupled thermal-elastic-plastic-damage model for concrete subjected to dynamic loading,” *International Journal of Plasticity*, vol. 153, 2022.
[27] B. Indraratna, S. Thirukumaran, E. T. Brown, W. Premadasa, and W. Gale, “A technique for three-dimensional characterisation of asperity deformation on the surface of sheared rock joints,” *International Journal of Rock Mechanics and Mining Sciences*, vol. 70, pp. 483–495, 2014.
[28] Q. Jiang, X. Feng, Y. Gong, L. Song, S. Ran, and J. Cui, “Reverse modelling of natural rock joints using 3D scanning and 3D printing,” *Computers and Geotechnics*, vol. 73, pp. 210–220, 2016.
[29] S. Huang, Y. Cai, Y. Liu, and G. Liu, “experimental and theoretical study on frost deformation and damage of red sandstones with different water contents,” *Rock Mechanics and Rock Engineering*, vol. 54, no. 8, pp. 4163–4181, 2021.
[30] M. Zhai, H. Bai, and L. Wu, “Shear slip instability behavior of rock fractures under prepeak tiered cyclic shear loading,” *Advances in Civil Engineering*, vol. 2020, Article ID 8851890, 12 pages, 2020.
[31] S. Mehrishal, M. Sharifzadeh, J.-J. Song, and K. Shahriar, “An investigation of the possibility of estimating the residual shear strength of rough joints using planar small joint in limestone rocks,” *Journal of Structural Geology*, vol. 142, Article ID 104220, 2021.
[32] K. Zhao, D. Yang, P. Zeng et al., “Effect of water content on the failure pattern and acoustic emission characteristics of red sandstone,” *International Journal of Rock Mechanics and Mining Sciences*, vol. 142, Article ID 104709, 2021.
[33] Z. Xu, Y. Luo, J. Chen, Z. Su, T. Zhu, and J. Yuan, “Mechanical properties and reasonable proportioning of similar materials in physical model test of tunnel lining cracking,” *Construction and Building Materials*, vol. 300, Article ID 123960, 2021.
[34] D. X. Xuan, L. J. M. Houben, A. A. A. Molenaar, and Z. H. Shui, “Mechanical properties of cement-treated aggregate material—a review,” *Materials & Design*, vol. l, no. 33, pp. 496–502, 2012.
[35] A. Roy, E. Perfect, W. M. Dunne, and L. D. McKay, “Fractal characterization of fracture networks: an improved box-counting technique,” *Journal of Geophysical Research*, vol. 112, no. B12, 2007.
[36] J. Liu, F. Gao, Y. Xing, W. Zheng, and Y. Bai, “A new 3D statistical parameter for determining roughness of joint surfaces considering shear direction and asperity features,” *KSCE Journal of Civil Engineering*, vol. 27, no. 11, pp. 4978–4992, 2023.
[37] N. Barton, “Suggested methods for the quantitative description of discontinuities in rock masses,” *ISRM, International Journal of Rock Mechanics and Mining Sciences & Geomechanics Abstracts*, vol. 15, pp. 319–368, 1978.
[38] G. Grasselli, J. Wirth, and P. Egger, “Quantitative three-dimensional description of a rough surface and parameter evolution with shearing,” *International Journal of Rock Mechanics and Mining Sciences*, vol. 39, no. 6, pp. 789–800, 2002.
[39] Z. Lianheng, H. Dongliang, C. Jingyu et al., “A practical photogrammetric workflow in the field for the construction of a 3D rock joint surface database,” *Engineering Geology*, vol. 279, Article ID 105878, 2020.